Crustal-scale shear zones and heterogeneous structure beneath the North Anatolian Fault Zone, Turkey, revealed by a high-density seismometer array

Metin Kahraman[1], David G. Cornwell[2,*], David Thompson[2,3], Sebastian Rost[3], Gregory Houseman[3], Niyazi Türkelli[1], Uğur Teoman[1], Selda Altuncu Poyraz[1], Murat Utkucu[4] and Levent Gülen[4]

[1] Kandilli Observatory and Earthquake Research Institute, Department of Geophysics, Boğaziçi University, 34684 Çengelköy, Istanbul, Turkey

[2] Department of Geology and Petroleum Geology, School of Geosciences, University of Aberdeen, King's College, Aberdeen, AB24 3UE

[3] School of Earth and Environment, University of Leeds, Leeds LS2 9JT, UK

[4] University of Sakarya Department of Geophysics, Sakarya University, Esentepe Campus, 54187, Serdivan, Sakarya, Turkey

* Corresponding author (Email: d.cornwell@abdn.ac.uk. Tel: +44 (0) 1224 3448)

Abstract

Continental scale deformation is often localized along strike-slip faults constituting considerable seismic hazard in many locations. Nonetheless, the depth extent and precise geometry of such

faults, key factors in how strain is accumulated in the earthquake cycle and the assessment of seismic hazard, are poorly constrained in the mid to lower crust. Using a dense broadband network of 71 seismic stations with a nominal station spacing of 7 km in the vicinity of the 1999 Izmit earthquake we map previously unknown small-scale structure in the crust and upper mantle along this part of the North Anatolian Fault Zone (NAFZ). We show that lithological and structural variations exist in the upper, mid and lower crust on length scales of less than 10 km and less than 20 km in the upper mantle. The surface expression of the NAFZ in this region comprises two major branches; both are shown to continue at depth with differences in dip, depth extent and (possibly) width. We interpret a <10 km wide northern branch that passes downward into a shear zone that traverses the entire crust and penetrates the upper mantle to a depth of at least 50 km. The dip of this structure appears to decrease west-east from ~90° to ~65° to the north over a distance of 30 to 40 km. Deformation along the southern branch may be accommodated over a wider (>10 km) zone in the crust with a similar variation of dip but there is no clear evidence that this shear zone penetrates the Moho. Layers of anomalously low velocity in the mid crust (20-25 km depth) and high velocity in the lower crust (extending from depths of 28-30 km to the Moho) are best developed in the Armutlu-Almacik block between the two shear zones. A mafic lower crust, resulting possibly from ophiolitic obduction or magmatic intrusion, can best explain the coherent lower crustal structure of this block. Our images show that strain has developed in the lower crust beneath both northern and southern strands of the North Anatolian Fault. Our new high resolution images provide new insights into the structure and evolution of the NAFZ and show that a small and dense passive seismic network is able to image previously undetectable crust and upper mantle heterogeneity on length lateral scales of less than 10 km.

1. Introduction

Major continental strike-slip faults, such as the North Anatolian fault Zone (NAFZ) in Turkey or the San Andreas Fault in the USA, are key elements in our understanding of plate tectonics. Such faults are clearly defined at the surface but considerable uncertainty surrounds their structure in the mid to lower crust and upper mantle, and specifically how deformation is focussed in shear zones that are presumed to extend beneath seismically active fault planes (e.g., Handy *et al.*, 2007; Platt and Behr, 2011). An understanding of such fault systems (e.g., Pollitz *et al.*, 2001) requires characterisation of the structure and physical properties of the crust and upper mantle to constrain the rheological parameters that determine how stress is redistributed during the earthquake cycle (e.g., Hearn *et al*., 2009). Localized zones of relatively high or low viscosity can have an important impact on this cycle (Yamasaki *et al.*, 2014).

Modelling of geodetic deformation has provided some constraints on the physical variation of creep parameters (e.g., Bürgmann and Dresen, 2008; Hearn *et al*., 2009; Kenner and Segall, 2003; Wright *et al.*, 2013), however, seismic imaging is the only method that can provide direct insights into the structure of the crust and the variation of elastic properties within it, albeit at length scales that are limited by the seismic wavelength. For instance, variations in Moho topography have been used to argue for both diffuse deformation within the crust (Wilson *et al*. 2004) and focussed fault structure in the upper mantle (e.g., Wittlinger *et al*., 2004). Such arguments require careful control on the velocity variation within the entire crustal section (Schulte-Pelkum and Ben-Zion, 2012). While geodetic measurements reveal short-term strains caused by the current earthquake cycle, seismological imaging can reveal details of the geological structures created by the cumulative effect of many earthquake cycles.

In this study, we use teleseismic receiver functions (RFs) to image crust and upper mantle structure across part of the NAFZ using seismological data recorded by a rectangular array with a station interval of ~7 km that was deployed for 18 months.

68 The NAFZ is a 1500 km-long right-lateral transform fault that separates a westward moving
69 Anatolia from a relatively stationary Eurasian plate (Fig. 1). Subduction along the Hellenic trench
70 and collision of the Arabian and Eurasian plates results in a general westward movement of
71 Anatolia at rates of 20-30 mm/yr relative to Eurasia (e.g. Barka, 1996; McClusky *et al.*, 2000;
72 Reilinger *et al.*, 2006), with strain focussed on the NAFZ. Numerous major earthquakes have
73 occurred during the last century (e.g. Barka, 1999); most recently in 1999 with epicentres at Izmit
74 and Düzce (e.g. Barka *et al*., 2002; Fig. 1). We installed a dense network (DANA - Dense Array for
75 Northern Anatolia) of temporary broadband seismic stations across the NAFZ in the region of the
76 1999 Izmit rupture in order to create exceptionally well-resolved images of NAFZ crustal structure.

77

78 ***2. Geological Overview***

79 The western NAFZ bisects a complex assembly of heterogeneous zones of differing crustal affinity,
80 namely the continental fragments of the Istanbul-Zonguldak Zone (IZ) and the Sakarya Zone (SZ)
81 (Fig.1) that form part of what is commonly referred to as the Pontides (e.g. Okay and Tüysüz,
82 1999). The IZ has a late Precambrian crystalline basement (Chen *et al.*, 2002; Yiğitbaş *et al.*, 2004;
83 Ustaömer *et al.*, 2005) unconformably overlain by a continuous Ordovician-Carboniferous
84 sedimentary succession (Görür *et al*., 1997; Dean *et al.*, 2000). Carboniferous convergent
85 deformation was followed by a Triassic marine transgression as the IZ formed part of the Laurasia
86 passive continental margin (Okay, 2008) before Late Cretaceous back-arc spreading created the
87 western Black Sea basin by rifting the present-day IZ southwards (Okay et al., 1994). The Intra-
88 Pontide Ocean gradually closed by north-dipping subduction during Late Cretaceous-Early Eocene
89 times (Okay and Tüysüz, 1999), forming the 400 km long east-west trending Intra-Pontide suture,
90 which is now reactivated as the present-day trace of the NAFZ (e.g. Okay and Tüysüz, 1999; Sengor
91 and Yilmaz, 1981; Okay, 2008). To the south, the basement of the SZ continental fragment consists

of widespread subduction-accretion complexes of Triassic age (Şengor and Yilmaz, 1981; Okay and Tüysüz, 1999). A Jurassic-Eocene sequence of clastic sedimentary, carbonate and volcanic rocks unconformably rests upon the high-grade metamorphic basement (Okay *et al*., 1996; Pickett and Robinson, 1996; Okay and Tüysüz, 1999).

West of about 30.65°E, the NAFZ splits into northern (NNAF) and southern (SNAF) strands with ~16 and ~9 mm/yr slip, respectively (e.g. Stein *et al.*, 1997). The Armutlu-Almacik crustal block (AA) lies between the NAFZ strands and is comprised of SZ pre-Jurassic basement (typically Triassic subduction/accretion units), SZ Jurassic-Eocene sedimentary sequences, a Cretaceous-Palaeocene accretionary complex and metamorphic rocks of unknown age and origin (possibly IZ; Sengor and Yilmaz, 1981; Okay and Tüysüz, 1999; Okay, 2008). The Sakarya River, offset in a right-lateral sense by the NAFZ, has incised the SZ and AA and has played a prominent role in erosion and deposition of sub-aerial clastic sediments that fill Neogene-Quaternary pull-apart basins near Adapazarı and Düzce (Barka and Gülen, 1988).

The complex accretion history that predates the development of the NAFZ leads us to expect a complex crustal structure in this region, but identifying contrasts in structure from one crustal block to another may reveal the cumulative impact of fault displacements and distributed shear across the fault zone.

3. Previous Geophysical Studies

Previous RF studies (Zor et al., 2006; Vanacore *et al.*, 2013) east of the Marmara Sea (Fig. 1) determined crustal thickness in the study region to increase from west (29-32 km) to east (34-35 km), with an average crustal V_P/V_S of ~1.75 (Vanacore *et al.*, 2013). A recent study used transfer functions to find a similar crustal thickness (30-35 km) beneath the majority of the DANA network,

115 with exceptionally thick (40-45 km) crust beneath north-western stations (Frederiksen *et al*., 2015).
116 Two seismic refraction experiments that spanned the NAFZ (Fig. 1) reported similar crustal
117 thicknesses of 32±2 km in the west (Bekler *et al.*, 2008) and ~38 km (Karahan, et al., 2001) in the
118 east of our study region, both sampling the AA, SZ and IZ blocks. Bekler *et al.* (2008) interpreted
119 an upper crustal layer (V_P=5.6-6.1 km/s) extending to ~5 km and lower crustal velocities of V_P=6.7-
120 7.2 km/s, above a low velocity (V_P=7.6 km/s) upper mantle on the western line. On the eastern
121 line, Karahan et al. (2001) found similar crustal velocities (though the upper layer extends to ~12
122 km depth) and mantle velocities of ~8.1 km/s. These investigations also identified possible crustal
123 seismic discontinuities at depths of ~17 km and ~24 km.

124 The crust of the IZ and AA appears to have relatively high velocity and low attenuation based on
125 local earthquake tomography (Koulakov *et al.*, 2010). Further along the NAFZ to the east (at 35°E,
126 41°N), local earthquake tomography revealed high-velocities (V_P=6.2-6.5 km/s at depths of 10 to
127 20 km) and large lateral variations in V_P/V_S ratios (1.72-1.80) in the mid-crust, attributed to varying
128 lithology and fluid content in the basement (Yolsal-Çevikbilen *et al.*, 2012).

129 Body wave tomography based upon simultaneous full waveform inversion of regional and
130 teleseismic waves (Fichtner *et al.*, 2013) and surface waves (Salaün *et al.*, 2012) shows relatively
131 fast velocities (δV_P=+2-3 %; δV_S=+3-4 %) within the IZ lithosphere to depths of at least 60 km
132 (Fichtner *et al.*, 2013) and possibly to 100-150 km. These high velocities appear to abruptly
133 terminate beneath the NAFZ (Berk Biryol *et al.*, 2011). Relatively slow upper mantle velocities
134 (δV_S=-3-4 %) underlie the SZ to the south of the NAFZ and a shallow asthenosphere is thought to
135 cause a broad region of low ($\delta V_S \leq$-2 % or V_S<4.2 km/s) velocity at depths ~100 km beneath the
136 majority of the NAFZ in Anatolia (Fichtner *et al.*, 2013).

137 Magnetotelluric (MT) data also show first order differences in the conductivity structure of the
138 crust from south to north across the NAFZ (Tank *et al*., 2005). A highly resistive (>1000 Ωm) crustal

basement in the IZ to the north and a moderately resistive crustal basement (>500 Ωm) in the SZ to the south flank a conductive (30-50 Ωm) region within the AA block that extends in depth between ~10 km and ~50 km, apparently into the upper mantle. This lower crustal conductive zone is interpreted as resulting from fluids created by metamorphic dehydration and/or partial melt in the upper mantle beneath the NAFZ (Tank *et al*., 2005).

4. Receiver Function Data and Calculation

The Dense Array for North Anatolia (DANA; Fig. 1), with a nominal inter-station spacing of 7 km and covering a region of 70 by 35 km along 6 north-south lines and 11 east-west lines (Fig 1), was operational from May 2012 until October 2013. An additional 7 stations formed a semi-circle of radius ~60 km around the rectangular array on its eastern side (Fig. 1). Three permanent stations of Boğaziçi University - Kandilli Observatory and Earthquake Research Institute/National Earthquake Monitoring Center (BU-KOERI/NEMC) contributed to the rectangular array. Using data recorded by DANA, we computed RFs from records of teleseismic earthquakes identified from the National Earthquake Information Center (NEIC) catalogue, with m_b>5.5 and angular distances of 30° to 90° (Fig. 2a). For completeness, RFs with maximum frequency of 1.2 Hz were estimated using two different techniques: the time domain iterative deconvolution approach (Ligorria and Ammon, 1999) (TDRFs); and extended-time multi-taper frequency domain cross-correlation (Helffrich, 2006) (MTRFs). TDRFs were used for *H-κ* stacking and depth migration analyses, whereas MTRFs were preferred for the RF inversion. We demonstrate the similarity and compatibility of the two RF calculation techniques in Supplementary Figure 1. A 2-way 2-pole high pass filter was applied to all RFs to suppress noise with frequencies less than 0.1 Hz. Calculated RFs were visually inspected and accepted if: 1) there is an absence of pre-signal noise (MTRFs only) on the radial and transverse RF; 2) transverse RFs show less (or comparable) amplitudes than radial RFs; 3) the

direct P-arrival is visible and close to predicted arrival time; and 4) there is no evidence of large amplitude oscillatory noise (i.e. "ringing"). This procedure resulted in post quality control TDRF and MTRF datasets consisting of 1363 and 2479 earthquake-station pairs, respectively. Figure 2 shows event locations, MTRF station stacks for all events used and RF stacks for the 6 sub-sections defined in Figure 3. The majority of recorded events occurred in an arc from north to east of the DANA array and few events sample other back-azimuthal directions (Fig. 2a). Such an event distribution limits the application of the dataset to RF azimuthal analysis (i.e. anisotropic or dipping layer) and we therefore focus here on the lateral variation in the isotropic crustal structure of this region (we also include regional back-azimuthal plots of radial and tangential MTRFs in Supplementary Figure 2).

The dense station spacing and event distribution provides excellent sampling of the crustal structure (Fig. 3). RF piercing point locations at a depth of 35 km were calculated using the IASP91 Earth model (Kennett and Engdahl, 1991) and RF stacks (Fig. 2c) were created by binning RFs by piercing point (Fig. 3), correcting for time moveout (to an angular distance of 65° using IASP91) and linearly stacking in six sub-regions. The sub-regions were chosen to examine first order variations in the crust defined by where the NAFZ dissects the three main crustal terranes: SW and SE stacks sample SZ crust to the south of the southern NAFZ branch; CW and CE stacks sample the central AA block defined by the NAFZ branches; and NW and NE stacks sample IZ crust north of the northern NAFZ branch.

5. H-κ Stacking Method and Results

H-κ stacking (Zhu and Kanamori, 2000) was performed using stacks of between 97 and 285 TDRFs with frequencies of up to 1.2 Hz from each of the six sub-regions outlined in Figure 3. The

technique produces estimates of crustal thickness (H) and average crustal V_P/V_S (κ) by stacking amplitudes at the predicted times of the Moho *P-S* conversion and its multiples for different values of H and κ. An average crustal *P* wave velocity of 6.2 km/s was assumed, based on *P* wave velocity models derived from the nearby (Fig. 1) seismic refraction experiments of Karahan *et al*. (2001) and Bekler et al. (2008).

The six regional H-κ stacks (Fig. 4) show minor variations in crustal thickness. We find H = 35 ± 2 km with average crustal V_P/V_S of 1.73 ± 0.05 for the SW stack (consisting of 111 TDRFs), in contrast to 34 ± 1 km and 1.85 ± 0.05 for the SE stack (171 TDRFs). Both regions show clear maxima in the H-κ stack, allowing precise determination of the crustal properties and good agreement between predicted traveltimes for Moho converted and reverberated energy.

The H-κ stack for the CE region (108 TDRFs) also shows a clear maximum, with a slightly greater crustal thickness of 37 ± 1 km but reduced average crustal V_P/V_S of 1.70 ± 0.04, whereas the CW stack (97 TDRFs) does not show a clear single maximum. We interpret the Moho from the maximum at H = 37 ± 1 km and V_P/V_S = 1.69 ± 0.04 but note a second maximum occurs at an H and V_P/V_S of 32 km and 1.82, respectively.

To the north of the northern NAFZ branch we find H = 37 ± 1 km and average crustal V_P/V_S of 1.73 ± 0.05 for the NW stack (236 TDRFs) and H = 39 ± 1 km and average crustal V_P/V_S of 1.73 ± 0.04 for the NE stack (285 TDRFs). A clear single maximum is observed in the NE H-κ stack whereas another double maxima result is obtained for the NW region, with the secondary maximum at H = 31 km and V_P/V_S = 1.86. We also find a maximum in the NW stack corresponding to a phase conversion at 55-60 km that is absent in the other regional TDRF stacks, indicating possible sub-crustal structure.

Overall, the H-κ stacking analysis demonstrates that the crustal thickness increases from south (34-35 km) to north (37-39 km) and the crustal thickness in the IZ increases by 1-2 km thicker from

west to east across the DANA region, similar to estimates obtained by Frederiksen *et al*., (2015). Estimates of average crustal V_P/V_S are typically ~1.70, except for an anomalous result of 1.85 in the SE sub-region.

6. Neighbourhood Algorithm Inversion Method and Results

We inverted the six regional MTRF stacks for velocity structure using the neighbourhood algorithm of Sambridge (1999). The inversion scheme attempts to find the velocity model that gives the best fit between the synthetic RF generated from the model and the actual stack. For each inversion, a seven layer parameter space (with search limits defined in Table 1) based upon the velocity model of Bekler *et al.* (2008) was searched using 10001 iterations with 13 initial samples and 13 Voronoi cells resampled at each iteration (see Sambridge, 1999 for details).

The inversion results for the six regional stacks are shown in Fig. 5 and Table 2. All inversion results for the six regional stacks show a good fit (with chi-squared misfit 0.063-0.074) to the observed MTRF stacks. We find evidence across the study region for a thin (<1.5 km) low velocity (V_S=1.8-2.3 km/s, V_P/V_S=1.72-1.96) layer at the surface underlain by a rapid transition to typical upper crustal (3.3-3.5 km/s) *S* wave velocities and V_P/V_S ratios of 1.68-1.81 below depths of 2.2-5.9 km. All regions show mid-crustal *S* wave velocities of 3.5-3.7 km/s (V_P/V_S=1.72-1.81), which may extend to Moho depths in the NW, SW and SE regions.

In the CW, CE and NE regions, however, a 10-13 km thick, relatively high velocity (V_S=3.9-4.2 km/s; V_P/V_S=1.67-1.74) lower crust is found, corresponding to a weakly positive conversion observed in the migrated TDRF images described in the following section. The Moho discontinuity is determined at depths between 33 and 39 km for the NW, NE, CW and CE regions, though ah more gradational velocity increase (albeit less than 4 km thick) may exist at the Moho beneath the SW

and SE regions (Moho depths: NW=36.8 km; NE=38.7km; CW=36.7 km; CE=36.6 km; SW=32.6-35.6 km; SE=34.7-38.6 km). Uppermost mantle velocities were consistent in all inversion results at V_S=4.4-4.5 km/s and V_P/V_S=1.70-1.75.

In summary, the inversion results support the inference of a generally thicker crust beneath the AA and eastern IZ crustal terranes (36-39 km) compared to the SZ terrane (33-39 km), in generally good agreement with the *H-κ* stacking results. Velocities in the lower crust are generally greater beneath the AA and IZ terranes (though not for the western IZ). Mantle velocities are typically lower than the global average.

7. Receiver Function Depth Migration

7.1. Method

We created migrated depth images of discontinuities beneath the DANA array by binning TDRFs according to their piercing points at 35 km depth (e.g. Dueker and Sheehan, 1997). In order to construct representative 2-D profiles we used a bin width of 15 km (similar to an estimated first Fresnel zone width of 14.8 km) perpendicular to the profile and 7.5 km along profile and linearly stack TDRFs within each bin. We utilized a laterally varying velocity model defined by our MTRF inversion results (Table 2) in the migration process (profiles migrated with *H-κ* stacking velocity results are shown in Supplementary Figure 3 for comparison). We present two south-north and three west-east profiles through the sub-surface volume sampled by the DANA array (Fig. 6). The western and eastern profiles sample the southern and northern strands of the NAFZ, while the three east-west profiles sample the three major tectonic blocks in the study area (SZ, AA and IZ, respectively) (Figs. 1 and 3).

7.2. Results: Western Profile

Substantial lateral changes in the crust and upper mantle are evident along the ~100 km long western profile (Fig. 6a). Little evidence for low velocity near surface sediments exists on the southern section of the profile since the deconvolved *P* arrival aligns well with zero time. As the northern branch of the NAFZ is crossed the *P* arrivals are offset from zero time near the surface location of the NNAF (Figs. 2 and 5a), most likely due to low velocity material filling a ~10-15 km wide basin. Further to the north, the upper crust of the IZ is characterised by strongly negative amplitudes, possibly denoting a low velocity layer (consistent with the findings of Frederiksen et al., 2015).

In the central section (at distances of -10 to 15 km) of the western profile (Fig. 6a), pronounced negative TDRF amplitudes may indicate the top of a low-velocity layer in the mid-crust (~17 km depth). This feature is confined to the AA block, as defined by the surface locations of the fault branches, and is underlain by a positive conversion (at ~25 km depth) that most likely signifies an increase in velocity and/or density in the lower crust. Strongly negative amplitudes occur elsewhere in the lower crust (particularly at distances of -40 to -30 km and 20 to 35 km and depths of 22-28 km). The major gap in this negative feature occurs immediately to the south of the SNAF (at distances of -25 to -15 km), where TDRF amplitudes appear dimmed throughout the entire crust (Fig. 6a).

The Moho can be clearly identified along the majority of the western profile at depths of ~32-34 km but its *P*-to-*S* conversion amplitude decreases from south to north (Fig 6a). An increase in lower crustal velocity just south of the SNAF may explain the observed amplitude decrease (over a horizontal distance of ~45 km). The Moho is deepest (~34 km) beneath the AA block and exhibits decreased amplitude beneath the IZ block further north. The Moho can be traced to the end of the profile at a depth of ~32-33 km despite its decreasing amplitude.

Deeper (sub-Moho) structures are clearly defined beneath the IZ block (distance 10 to 40 km) and are characterized by high TDRF amplitudes, both positive (at 45-50 km depth) and negative (60-70 km depth). These features commence and are shallowest within 5 km of the surface location of NNAF and deepen northwards to the end of the western profile. Sub-Moho conversions beneath the AA and SZ parts of the western profile are only weakly evident (Fig. 6a).

In general, both fault strands are clearly evident in the western section, coinciding with major changes in crustal and upper mantle structure. We observe localized relatively low amplitudes associated with both fault strands; notably migrated TDRFs within ~15 km of the SNAF (Fig. 6a, distance -25 to -10 km) have relatively low amplitudes and are relatively featureless compared to the higher amplitude signatures from the crust elsewhere beneath the section. The most likely cause of the low amplitude signals close to the fault traces is attenuation and/or scattering of the converted waves due to near-surface (or near-station) heterogeneity and/or deformation caused by faulting in the brittle upper crust.

7.3. Results: Eastern Profile

In contrast to the western profile, the crustal structure along the eastern profile (Fig. 6b) appears to be generally less complex with lesser amplitudes. The main evidence for near surface low velocity layers is found in the area north of the NNAF (north of 5 km distance) along this profile. In the AA (-15 to 0 km) and SZ (south of -25 km), we detect low migrated TDRF amplitudes, similar to those observed in the SZ of the western profile. Strongly negative amplitudes exist at depths of 10 to 13 km immediately south of the SNAF (distance -25 to -10 km) and at depths of 5 to 10 km at a distance of 15-20 km north of the NNAF, respectively, possibly indicating the top of a low velocity layer at these locations.

The most striking feature of the eastern profile (Fig. 6b) is a positive lower crustal conversion (at 25-28 km depth) that extends laterally for ~50 km (distance -25 to 20 km). It lies beneath a weak negative conversion at 18-23 km depth and appears to be the same discontinuity that can be identified on the western profile, corresponding to a region of increased velocity and/or density in the lower crust. However, instead of being confined to the AA crust, it appears to extend from -30 km to 20 km on the migrated profile. Moderate to strong negative amplitudes, perhaps indicative of a low velocity layer, characterize the lower crust to the north of this feature (25 to 45 km distance). In the SZ to the south of it (-40 to -30 km distance), migrated TDRF amplitudes appear weak throughout the lower crust.

The Moho dips to the south; with depths of 37-38 km, 36-37 km and 32-34 km beneath the southern (SZ), central (AA) and northern (IZ) sections of this profile, respectively. As in the western profile, Moho *P*-to-*S* conversion amplitudes decrease from south to north. Sub-Moho signals are weakly positive and negative north of distance 35 km (Fig. 6b), dipping northwards at depths of 45-50 and 50-55 km, respectively.

7.4. Results: Southern Profile

The three ~50 km long west-east profiles (Figs. 6c-e) all display clear evidence for lateral variations in crustal structure. The southern profile (Fig. 6c) samples the SZ crust and it appears less complex than the central and northern profiles described below. We do not find clear evidence for a near-surface low velocity layer but detect a moderately negative upper crustal conversion (10-15 km depth) in the eastern part of the profile (0 to 25 km distance).

High amplitude negative phases at -20 to -5 km distance may reveal a low velocity lower crust whereas positive conversions at a depth of ~30 km at positive profile distances likely correspond to the top of the high velocity and/or density lower crust as observed in the southern part of the

eastern profile (Fig. 6b).

The Moho depth varies from ~32 km in the west of the southern profile (-20 to -10 km distance) to 36-38 km in the central and eastern sections (-5 to 25 km distance). It is characterized by strong *P*-to-*S* conversion amplitudes that decrease slightly in the central 10 km of the profile (Fig. 6c). There is little evidence for sub-crustal heterogeneity beneath the southern profile.

7.5. Results: Central Profile

The central profile (Fig. 6d) samples the AA block. There is no clear evidence for a substantial near-surface low-velocity layer along this profile. The mid-crust, however, is dominated by high amplitude negative conversions that rise from a depth of ~17 km in the western part (-20 to 0 km distance) to ~13 km in the centre (distance -10 to 0 km). At distances of 5 to 30 km distance, the mid-lower crust displays weakly negative *P-S* conversions at 18 to 22 km depth.

A distinctive feature of this profile is the positive amplitude signal that defines the top of a variable thickness lower crustal layer at depths of ~27, ~22 and ~26 km in the western, central and eastern sections of the profile, respectively (Fig. 6d, dashed red line). Combined with a varying Moho depth, this relatively high velocity and/or high density layer at the base of the crust has a thickness of 6-13 km.

The Moho is predominantly at a depth of 31-33 km along this profile, but can reach ~35 km beneath at distances of -10 to 5 km. There is no clear evidence for sub-Moho arrivals along the central profile from the migrated TDRFs.

7.6. Results: Northern Profile

The northern profile highlights strong east-west variations in the crustal structure of the IZ (Fig. 6e). TDRF *P* arrivals are offset from zero time (as observed in the IZ section of the western profile discussed in section 7.2) at distances of -20 to 0 km, indicative of a substantial (>2 km thick) near-surface low velocity layer. The upper and lower crust along the northern profile generally lacks any strong *P*-*S* converted energy, with near-zero amplitudes present in all but the easternmost TDRF migrated stack (at 15 km distance).

A relatively weak Moho *P*-to-*S* conversion is present at a depth of ~32 km in the centre of the profile (-10 km distance), deepening eastwards to ~35 km. Larger amplitude positive and negative conversions at occur at depths of 45-50 km and ~65 km, respectively in the western part of this profile (Fig. 6e, -30 to -10 km distance). These sub-Moho arrivals, also identified in the northern parts of the eastern and western profiles, possibly extend eastwards with greatly reduced amplitudes.

8. Discussion

The short station separation (~7 km) of the DANA array has enabled us to detect strong variations in crustal structure and properties despite the relatively small footprint of this study compared to other broadband seismological studies. *H*-*κ* analysis and neighbourhood algorithm inversion results indicate structural changes both in north-south (across the surface expression of the faults) and east-west directions. The Moho can be detected in most regions and shows measurable variations in depth and velocity contrast on scale lengths of 5 to 10 km. Our high resolution migrated RF images (Fig. 6) detail a heterogeneous crust and upper mantle, with the main structural changes correlated to the surface expression of the NNAF and SNAF strands.

8.1. The northern fault strand (NNAF)

The northern branch of the North Anatolian Fault Zone (NNAF) was the locus of the disastrous 1999 Izmit earthquake (Fig. 1). The migrated RF images show truncations of crustal *P-S* converted phases in the AA and IZ terranes across the NNAF, respectively, and a disturbed Moho conversion is observed over a fault-perpendicular width of <10 km. Local earthquakes recorded during the DANA deployment (Altuncu Poyraz *et al.*, 2015) show that seismicity clusters in the upper 15 km of the crust vertically above these truncations and is strongest where co-seismic displacement of the 1999 event (Feigl *et al.*, 2002) is greatest. Continuing shear on the NNAF in the lower crust presumably occurs aseismically. Truncations of upper mantle lateral features vertically beneath the surface expression of the NNAF (Figs. 6a and 6b) suggests that localized shear of the NNAF to depths continues to depths of at least 50 km. Although lateral resolution of the RF migrated profiles limits our ability to discriminate between a fault or shear-zone with widths of less than ~10 km, the western profile (Fig. 6a) shows clear and direct evidence for a narrow zone of shear beneath the NNAF that passes through the entire crust and into the lithospheric mantle. The width of this shear zone (<10 km) is similar to the width of the most seismically active region in the upper crust (Fig. 6a; Altuncu Poyraz *et al.*, 2015) and is likely to be near vertical (Fig. 6a).

Along the eastern profile, truncated structures throughout the entire crust can also be identified. In contrast to the western profile, these truncations are displaced to the north of the surface trace of the NNAF by ~5 km in the upper crust, ~15 km in the mid-lower crust and 25-30 km in the upper mantle (Fig. 6b). In addition, a decrease in the depth and amplitude of the Moho occurs along this profile at ~15 km north of the NNAF (Fig. 6b), perhaps related to a change in (lower) crustal velocity. The upper mantle structure observed beneath the IZ is similar to that truncated by the NNAF on the western profile but these structures are not continuous and are situated at the limits of our resolution (Fig. 6b).

394 The local seismicity along the eastern profile (Altuncu Poyraz *et al.*, 2015) is more diffuse, probably
395 indicating a wider zone of upper crustal deformation than in the west. The more diffuse seismicity,
396 northward offset truncations of upper and lower crustal features and coherent lower crustal
397 positive amplitudes directly beneath the NNAF provide evidence that the NNAF at this longitude
398 passes through the crust as a 15-25 km wide zone of deformation. An equally plausible
399 interpretation of these observations is that a narrow (7-10 km wide) NNAF shear zone dips
400 northward at ~65°, traced by the truncated crust and upper mantle converted phases (Fig. 6b).
401 This interpretation is shown schematically in Fig. 7b.

402

403 *8.2. The southern fault strand (SNAF)*

404 Truncation of mid- and lower crustal AA block structures could be evidence for a SNAF that cuts
405 through most of the crust on the western profile (Fig. 6a). However, laterally continuous Moho
406 conversions may indicate that the SNAF does not pass into the upper mantle beneath this area. A
407 ~6 km wide region of relatively deep (<20 km) seismicity (Altuncu Poyraz *et al.*, 2015) may show a
408 narrow sub-vertical fault zone extending into the mid-crust. Alternatively, a ~15 km wide region of
409 anomalously low RF amplitudes and a cluster of events at shallower depths (<13 km) south of the
410 SNAF topographic low may signify a wider (<15 km) deformation zone within the crust (Fig. 6a).

411 Clear upper crustal polarity changes on the eastern profile coincide with the depth extent (<18 km)
412 and location of locally high rates of seismicity centred below the 'V' shaped valley that hosts the
413 SNAF (Fig. 6b). Deeper in the mid-lower crust, however, negative (at ~20 km depth) and positive
414 (at ~27 km depth) *P-S* conversions are continuous from ~15 km south of the SNAF to ~20 km north
415 of the NNAF. If the ~15 km southward offset in these truncations is attributed to a continuous
416 linear shear zone from the SNAF surface expression, a dip of ~65° southwards could be inferred

417 (Fig. 6b). On the other hand, weaker Moho *P-S* conversions beneath the SNAF-related seismicity
418 (at -25 to -5 km distance) may provide evidence for a sub-vertical zone of diffuse shear whose
419 width increases with depth beneath the SNAF (Fig. 6b). These contrasting interpretations are
420 shown in Fig. 7.

421

422 *8.3. East-west structural variation of terranes and fault zone*

423 The observed contrast in properties between IZ and SZ terranes was anticipated since the Intra-
424 Pontide suture marks the boundary between major crustal blocks of different provenance (e.g.
425 Okay and Tüysüz, 1999). We also demonstrate previously unknown east-west variations in crust
426 and upper mantle structure within each of the IZ and SZ terranes that are of similar magnitude to
427 variations observed across the NAFZ.

428 We find evidence for a major structural boundary separating east and west parts of the IZ terrane
429 beneath the DANA array (Fig. 6e), a concept that may be supported by a markedly different
430 sedimentary deposition record in the the study region (e.g. Okay *et al*., 1996). A southwest to
431 northeast trajectory separating these two regions would bound, if continued towards the Black
432 Sea, the northern edge of the exposed pre-Cambrian basement of the IZ (Yiğitbaş *et al.*, 2004) and
433 the near-linear southern Black Sea coastline near Zonguldak (Fig. 1).

434 Comparing crustal thickness of the western and eastern IZ, the NA inversion finds the east slightly
435 thinner; the *H-κ* algorithm finds the opposite, but also finds a secondary maximum for the NW
436 region. These differences may be attributed to greater velocities in the lower crust of the NE
437 region (Fig. 6). The sub-Moho structure at depths of 40-60 km beneath the IZ in our study region
438 could be the signature of remnant under-thrust oceanic or continental crust from the closure of an
439 Intra-Pontide ocean (e.g. Robertson and Ustaömer, 2004). It could also represent crust thickened

by an older tectonic event, such as thrusting and subduction related to the closure of the Tethys (e.g. Şengör and Yilmaz, 1981).

In comparison, the SZ crust and upper mantle are less complex and might be considered the stable block within the region. Our constrained crustal thickness estimates of 33-37 km (*H*-*κ*), 31-38 km (migrated RF images) and 36-39 km (inversion) are broadly consistent with each other and with previous seismic refraction experiments (32±2 km, Bekler *et al.*, 2008 and ~38 km, Karahan, *et al.*, 2001) but slightly deeper than previous estimates of 29-35 km using RFs (Zor *et al.*, 2006; Vanacore *et al.*, 2013). However, a first order change in crustal RF signature from west to east (Fig. 6c) suggests the possibility of two different crustal terranes comprising the SZ within the study region.

The possible change in dip of both SNAF and NNAF fault strands, from near vertical to ~65° over an east-west distance of only 25 km, is intriguing (Figs. 6a, 6b and 7) and further work is required to determine whether it may be a natural consequence of the two surface fault strands converging or that the NAFZ has locally re-activated a relatively complex structure inherited from the Intra-Pontide suture (e.g. Zor *et al.*, 2006).

8.3. Inferences for crustal rheology

We infer low velocities in the mid-crust in the AA block at depths of 15-23 km in the west and 19-27 km in the east of our study area (Fig. 6d) that correspond approximately to a mid-crustal low-viscosity zone interpreted by Yamasaki *et al*., (2014) in order to explain geodetic measurements of deformation before and after the 1999 Izmit earthquake.

The lower crust of the AA zone has a relatively high velocity; such velocities are typically interpreted as mafic granulite or as a layer containing solidified magmatic intrusions (e.g. Cornwell

et al., 2010). Lower crustal magmatic intrusions are less commonly described in large scale continental strike slip settings, although northern parts of the onshore San Andreas fault also exhibit a high velocity lower crust attributed to mafic intrusions (e.g. Henstock et al., 1997). High velocities in the lower crust of the AA block may also be compatible with the visco-elastic earthquake cycle model of Yamasaki *et al.* (2014) for which high viscosities in the lower crust are also inferred.

9. Conclusions

The high resolution imaging afforded by the dense station distribution of the DANA array allows unprecedented insight into the fine scale structure of a continental strike slip fault, detecting lateral changes in crustal structure over less than 10 km. Based on the structures detected in this study the two fault branches (NNAF and SNAF) of the North Anatolian Fault Zone appear to trace the locations of crustal-scale shear zones developed during the long history of displacement events. Truncation of crustal and upper mantle features in the RFs allows the depth extent of the faults mapped at the surface (or the narrow shear zones that extend down beneath them) to be determined.

The western parts of our study area show both fault zones dipping steeply. We can trace the NNAF into the upper mantle to a depth of at least 50 km, while the structure beneath the SNAF is more diffuse, a feature that may be associated with the observed lesser long-term strain rate on the southern strand. Only 25 km further east we interpret a much shallower dip of both fault strands. The NNAF in the lower crust could be as narrow as 10 km, while the SNAF is probably more diffuse and we do not see clear evidence that it cuts the Moho.

Furthermore, we have shown that lithologic variations exist in the upper, mid and lower crust over distances of less than 10 km and in the upper mantle over distances of less than 20 km. A simple interpretation of these variations is that they arise from the juxtaposition of crustal blocks from different provenances across relatively narrow shear zones. Localization of viscous strain can also produce the observed variations in density and depth of seismicity on and around the NAFZ. The identification of differences in dip, depth extent and (possibly) width of the two NAFZ branches along strike in the study region could indicate that greater strain localization has occurred on the northern strand of the NAFZ. The AA block between the two fault strands is characterized by a clearly distinct mid-crustal low velocity layer overlying a relatively high velocity lower crust.

Acknowledgments

DANA (Dense Array for Northern Anatolia) is part of the Faultlab project, a collaborative effort by the University of Leeds, Bogaziçi University Kandilli Observatory and Earthquake Research Institute (BU-KOERI) and Sakarya University. Major funding was provided by the UK Natural Environment Research Council (NERC) under grant NE/I028017/1. Equipment was provided and supported by the NERC Geophysical Equipment Facility (SEIS-UK). This project is also supported by Boğaziçi University Scientific Research Projects (BAP) under grant 6922 and Turkish State Planning Organization (DPT) under the TAM project, number 2007K120610. The authors thank the Editor, two anonymous reviewers and A. Arda Özacar for their comments which improved the manuscript.

11. References

1. Altuncu Poyraz, S., Teoman, U., Kahraman, M., Türkelli, N., Rost, S., Houseman, G., Thompson, D., Cornwell, D., Mutlu, A. K., Cambaz, D., Utkucu, M., Gülen, L., accepted 2015. New constraints on micro-seismicity and stress state in the western part of the North Anatolian Fault Zone: Observations from a dense seismic array, Tectonophysics**,** TECTO10106R2.
2. Barka, A. & Gülen L., 1988. New Constraints on Age and Total Offset of the North Anatolian Fault Zone: Implications for Tectonics of The Eastern Mediterranean Region. METU Journal of Pure and Applied Sciences, 21, 1-3, 39-63.
3. Barka, A. A., 1996. Slip distribution along the North Anatolian fault associated with the large earthquakes of the period 1939 to 1967, Bull. Seism. Soc. Am. 86, 1238–1254.
4. Barka, A., 1999. The 17 August 1999 Izmit earthquake, Science 285, 1858–1859.
5. Barka, A., S. Akyuz, E. Altunel, G. Sunal, Z. Cakir, A. Dikbas, B. Yerli, R. Armijo, B. Meyer, J. B. Chabalier, T. Rockwell, J. Dolan, R. Hartleb, T. Dawson, S. Christofferson, A. Tucker, T. Fumal, R. Langridge H. Stenner, W. Lettis, W. Page, and J. Bachhuber, 2002. The surface rupture and slip distribution of the 17 August 1999 Izmit earthquake (M 7.4), North Anatolian fault, Bull. Seism. Soc. Am. 92, 43–60.
6. Bekler, T., & Gokler, C., 2008. Insight into the Crustal Structure of the Eastern Marmara Region, NW Turkey, Pure and Applied Geophysics, 165, 295..
7. Berk Biryol, C., Beck, S., Zandt, G., Ozacar, A.A., 2011. Segmented African lithosphere beneath the Anatolian region inferred from teleseismic P-wave tomography. Geophys. J. Int. 184, 1037–1057.
8. Bürgmann, R., and G. Dresen (2008), Rheology of the lower crust and upper mantle: Evidence from rock mechanics, geodesy and field observations, Ann. Rev. Earth Plan. Sci., 36, doi:10.1146/annurev.earth.36.031207.124326, 531-567.

529 9. Chen, F., Siebel, W., Satir, M., Terzioğlu, N. & Saka, K., 2002. Geochronology of the Karadere
530 basement (NW Turkey) and implications for the geological evolution of the İstanbul Zone.
531 International Journal Earth Sciences, 91, 469-481.
532 10. Cornwell, DG., Maguire, PKH., England, RW. & Stuart, GW., 2010. Imaging detailed crustal
533 structure and magmatic intrusion across the Ethiopian Rift using a dense linear broadband
534 array, *Geochemistry, Geophysics, Geosystems*, vol 11, no. 1, Q0AB03.
535 11. Dean, W.T., Monod, O., Rickards, R.B., Demir, O. & Bultynck, P., 2000. Lower Palaeozoic
536 stratigraphy and palaeontology, Karadere-Zirze area, Pontus Mountains, northern Turkey,
537 Geological Magazine, 137, 555-582.
538 12. Dueker, K.G. & Sheehan, A.F. 1997. Mantle discontinuity structure from mid point stacks of
539 converted P to S waves across the Yellowstone hotspot track. Journal of Geophysical Research,
540 Vol. 102, No. B4, Pages 8313-8327.
541 13. Feigl, K. L., F. Sarti, H. Vadon, S. McClusky, S. Ergintav, P. Durand, R. Burgmann, A. Rigo, D.
542 Massonnet, and R. Reilinger,2002. Estimating slip distribution for the Izmit mainshock from
543 coseismic GPS, ERS-1, RADARSAT and SPOT measurements, Bull. Seismol. Soc. Am., 92(1),
544 138– 160.
545 14. Fichtner, A., Saygin, E., Taymaz, T., Cupillard, P., Capdevillee, Y., Trampert, J., 2013. The deep
546 structure of the North Anatolian Fault Zone, Earth Planet. Sci. Lett. 373, 109–117.
547 15. Frederiksen, A.W., Thompson, D.A., Rost, S., Cornwell, D.G., Gulen, L., Houseman, G.A.,
548 Kahraman, M., Altuncu Poyraz, S.A., Teoman, U.M., Turkelli, N. & Utkucu, M. (2015). 'Crustal
549 thickness variations and isostatic disequilibrium across the North Anatolian Fault, western
550 Turkey'. *Geophysical Research Letters*, vol 42, no. 3, pp. 751-757.
551 16. Görür, N., Monod, O., Okay, A.I., Şengör, A.M.C., Tüysüz, O., Yiğitbaş, E., Sakinç, M. & Akkök,
552 R., 1997. Palaeogeographic and tectonic position of the Carboniferous rocks of the western
553 Pontides (Turkey) in the frame of the Variscan belt. Bulletin Societe Géologique de France 168,

197-205.

17. Handy, M.R., Hirth, G., Bürgmann, R., 2007. Continental fault structure and rheology from the frictional-to-viscous transition downward. In: Handy, M.R., Hirth, G., Hovius, N. (Eds.), Tectonic Faults: Agents of Change on a Dynamic Earth. MIT Press, Cambridge, MA, pp. 139–181.
18. Hearn, E. H., S. McClusky, S. Ergintav, and R. E. Reilinger (2009), Izmit earthquake postseismic deformation and dynamics of the North Anatolian Fault Zone, J. Geophys. Res., 114, B08405, doi:10.1029/2008JB006026.
19. Helffrich, G., 2006. Extended-time multitaper frequency domain cross-correlation receiver-function estimation. Bull. Seism. Soc. Am. 96 (1), 344–347. doi:10.1785/0120050098.
20. Henstock, T.J., Levander, A. and Hole, J.A., 1997. Deformation in the lower crust of the San Andreas fault system in northern California. Science, 278, 650–653.
21. Karahan, A., Berckhemer, H. & Baier,B., 2001. Crustal structure at the western end of the North Anatolian Fault Zone from deep seismic sounding, *Annali di Geofisica,* **44,** 49–68.
22. Kenner, S.J. and Segall, P., 2003. Lower crustal structure in northern California: Implications from strain-rate variations following the 1906 San Francisco earthquake, J. Geophys. Res., 108. doi:10.1029/2001JB000189
23. Kennett, B. L. N. and E. R. Engdahl (1991). Travel times for global earthquake location and phase identification, *Geophys. J. Int.*, **105**, 429-465.
24. Koulakov, I., Bindi, D., Parolai, S., Grosser, H., Milkereit, C., 2010. Distribution of seismic velocities and attenuation in the crust beneath the North Anatolian Fault (Turkey) from local earthquake tomography. Bull. Seismol. Soc. Am. 100, 207–224.
25. Ligorria, J. P., and C. J. Ammon, Iterative deconvolution and receiver function estimation, *Bull. Seismol. Soc. Am.*, **89**, 1395–1400, 1999.
26. McClusky, S., S. Balassanian, A. Barka, C. Demir, S. Ergintav, I. Georgiev, O. Gurkan, M.

579 Hamburger, K. Hurst, H. Kahle, K. Kastens, G. Kekelidze, R. King, V. Kotzev, O. Lenk, S.
580 Mahmoud, A. Mishin, M., Nadariya, A. Ouzounis, D. Paradissis, Y. Peter, M. Prilepin, R.
581 Reilinger, I. Sanli, H. Seeger, A. Tealeb, M. N. Toksoz, and G. Veis, 2000. Global positioning
582 system constraints on plate kinematics and dynamics in the eastern Mediterranean and
583 Caucasus, J. Geophys. Res. 105, no. 3, 5695–5719.
584 27. Okay, A.I., Şengör, A.M.C.& Görür, N., 1994. Kinematic history of the opening of the Black Sea
585 and its effect on the surrounding regions. Geology, 22, 267-270.
586 28. Okay, A.I., Satir, M., Maluski, H., Siyako, M., Monie, P., Metzger, R. & Akyüz, S., 1996. Paleo-
587 and Neo-Tethyan events in northwest Turkey: Geological and geochronological constraints. In:
588 A. Yin & M. Harrison (eds.), Tectonics of Asia, Cambridge University Press, 420-441.
589 29. Okay, A.I., Tüysüz, O., 1999. Tethyan sutures of northern Turkey. Geol. Soc. London (Spec.
590 Publ.) 156, 475–515.
591 30. Okay, A. I., 2008. Geology of Turkey: A Synopsis, Anschnitt, 21, 19-42.
592 31. Pickett, E.A. & Robertson, A.H.F., 1996. Formation of the Late Paleozoic-Early Mesozoic
593 Karakaya Complex and related ophiolites in NW Turkey by Paleotethyan subduction accretion,
594 Journal of the Geological Society London, 153, 995-1009.
595 32. Platt, J.P., Behr, W.M.,2011. Deep structure of lithospheric fault zones. Geophys. Res. Lett.
596 38(24).
597 33. Pollitz, F.F, Wicks, C. Thatcher, W., 2001. Mantle flow beneath a continental strike-slip fault:
598 Postseismic deformation after the 1999 Hector Mine Earthquake, Science, 293, 1814-1818.
599 34. Reilinger, R., McClusky, S., Vernant, P., Lawrence, S., Ergintav, S., Cakmak, R., Ozener, H.,
600 Kadirov, F., Guliev, I., Stepanyan, R., Nadariya, M., Hahubia, G., Mahmoud, S., Sakr, K.,
601 ArRajehi, A., Paradissis, D., Al-Aydrus, A., Prilepin, M., Guseva, T., Evren, E., Dmitrotsa, A.,
602 Filikov, S.V., Gomez, F., Al-Ghazzi, R., Karam, G., 2006. GPS constraints on continental
603 deformation in the Africa- Arabia-Eurasia continental collision zone and implications for the

dynamics of plate interactions. J. Geophys. Res. 111, B05411, doi:10.1029/2005JB004051.

35. Robertson, A.H.F., Ustaömer, T., 2004. Tectonic evolution of the Intra-Pontide suture zone in the Armutlu Peninsula, NW Turkey, Tectonophysics, 381, 1–4, 175-209.

36. Salaün, G., Pedersen, H.A., Paul, A., Farra, V., Karabulut, H., Hatzfeld, D., Papazachos, C., Childs, D.M., Pequegnat, C., 2012. The SIMBAAD Team, 2012. High-resolution surface wave tomography beneath the Aegean-Anatolia region: constraints on upper-mantle structure. Geophys. J. Int. 190, 406–420.

37. Sambridge, M., Geophysical inversion with a Neighbourhood algorithm, I, Searching a parameter space, Geophys. J. Int., 138, 479–494, 1999.

38. Schulte-Pelkum, V. And Y. Ben-Zion, Apparent vertical Moho offsets under continental strike-slip faults from lithology contrasts in the seismogenic crust, Bull. Seis. Soc. Am. 102, 2757-2763, doi: 10.1785/0120120139, 2012.

39. Şengör, A.M.C. & Yilmaz, Y., 1981. Tethyan evolution of Turkey, a plate tectonic approach, Tectonophysics, 75, 181-241.Stein, R.S., Barka, A.A., Dieterich, J.H., 1997. Progressive failure on the North Anatolian Fault since 1939 by earthquake stress triggering. Geophys. J. Int. 128, 594–604.

40. Tank SB, Honkura Y, Ogawa Y, Matsushima M, Oshiman N, Tuncer MK, Celik C, Tolak E, Isikara AM, 2005. Magnetotelluric imaging of the fault rupture area of the 1999 Izmit (Turkey) earthquake, Phys. Earth. Planet. Int., 150, 213–225.

41. Ustaömer P.A., Mundil, R. & Renne, P.R., 2005. U/Pb and Pb/Pb zircon ages for arc-related intrusions of the Bolu Massif (W Pontides, NW Turkey): evidence for Late Precambrian (Cadomian) age, Terra Nova, 17, 215-223.

42. Vanacore, E., Taymaz, T., Saygin, E., 2013. Moho structure of the Anatolian plate from receiver function analysis. Geophys. J. Int. 193, http://dx.doi.org/10.1093/ gji/ggs107.

43. Wilson C.K., Jones C.H., Molnar P., Sheehan A.F., Boyd O.S., 2004. Distributed deformation in

the lower crust and upper mantle beneath a continental strike-slip fault zone: Marlborough fault system, South Island, New Zealand, Geology, 32, 837–840.

44. Wittlinger, G., Vergne, J., Tapponnier, P., Farra, V., Poupinet, G., Jiang, M., Su, H., Herquel, G., Paul, A., 2004. Teleseismic imaging of subducting lithosphere and Moho offsets beneath western Tibet. *Earth Planet. Sci. Lett*., 221, 117-130.

45. Wright TJ; Elliott JR; Wang H; Ryder I (2013) Earthquake cycle deformation and the Moho: Implications for the rheology of continental lithosphere, *Tectonophysics*, **609**, pp.504-523. doi: 10.1016/j.tecto.2013.07.029

46. Yamasaki T; Wright TJ; Houseman GA (2014). Weak ductile shear zone beneath a major strike-slip fault: inferences from earthquake cycle model constrained by geodetic observations of the western North Anatolian Fault Zone, Journal of Geophysical Research: Solid Earth, 119, pp.3678-3699. Doi: 10.1002/2013JB010347

47. Yiğitbaş, E., Kerrich, R., Yilmaz, Y., Elmas, A. & Xie, Q.L., 2004. Characteristics and geochemistry of Precambrian ophiolites and related volcanics from the İstanbul-Zonguldak Unit, Northwestern Anatolia, Turkey: following the missing chain of the Precambrian South European Suture zone to the east, Precambrian Research, 132, 179206.

48. Yolsal-Çevikbilen, S., Biryol, C.B., Beck, S., Zandt, G., Taymaz, T., Adiyaman, H.E., Özacar, H.E., 2012. 3-D crustal structure along the North Anatolian Fault Zone in north-central Anatolia revealed by local earthquake tomography. Geophys. J. Int. 188, 819–849.

49. Zhu, L. & Kanamori, H. 2000. Moho depth variation in southern California from teleseismic receiver functions. Journal of Geophysical Research, 105, 2969 – 2980.

50. Zor E., Sandvol E., Gürbüz C., Türkelli N., Seber D., Barazangi M., 2003. The crustal structure of the east Anatolian plateau (Turkey) from receiver functions, Geophys. Res. Lett., 30 (24), 8044, doi:10.1029/2003GL018192.

Layer	*Min. thickness (km)*	*Max. thickness (km)*	*Min. V_S top (km/s)*	*Max. V_S top (km/s)*	*Min. V_S base (km/s)*	*Max. V_S base (km/s)*	*Min. V_P/V_S*	*Max. V_P/V_S*	Q_P	Q_S
1	0	5	1.75	2.50	1.75	2.50	1.67	2.00	300	150
2	0.5	5	2.50	3.30	2.50	3.30	1.67	1.82	1450	600
3	0	15	3.30	3.50	3.30	3.50	1.67	1.82	1450	600
4	0	15	3.40	3.60	3.40	3.60	1.67	1.82	1450	600
5	0	15	3.50	3.70	3.50	3.70	1.67	1.82	1450	600
6	0	15	3.90	4.20	3.90	4.20	1.67	1.82	1450	600
7	5	30	4.45	4.70	4.45	4.70	1.70	1.75	1450	600

Table 1 – Details of the neighbourhood algorithm parameter space searched for the non-linear inversion for *S*-wave velocity structure (V_P, V_S, Q_P and Q_S denote *P*- and *S*-wave velocity and seismic quality, respectively).

	North-West RF Stack (NW)				**North-East RF Stack (NE)**			
Layer	*Thickness (Depth) (km)*	*V_S top (km/s)*	*V_S base (km/s)*	*V_P/V_S*	*Thickness (Depth) (km)*	*V_S top (km/s)*	*V_S base (km/s)*	*V_P/V_S*
1	1.2 (1.2)	1.77	1.91	1.72	0.8 (0.8)	1.76	2.21	1.96
2	2.4 (3.5)	2.82	3.22	1.68	1.2 (2.0)	2.66	3.14	1.68
3	9.0 (12.5)	3.48	3.47	1.74	1.8 (3.8)	3.32	3.41	1.68
4	9.3 (21.8)	3.60	3.44	1.72	9.7 (13.6)	3.56	3.49	1.82
5	14.9 (36.8)	3.53	3.67	1.74	14.1 (27.6)	3.59	3.65	1.76
6	14.3 (51.1)	3.91	4.19	1.82	11.1 (38.7)	3.92	4.13	1.74
7	23.6 (74.7)	4.46	4.45	1.74	16.0 (54.7)	4.46	4.46	1.75
	Central-West RF Stack (CW)				**Central-East RF Stack (CE)**			
Layer	*Thickness (Depth) (km)*	*V_S top (km/s)*	*V_S base (km/s)*	*V_P/V_S*	*Thickness (Depth) (km)*	*V_S top (km/s)*	*V_S base (km/s)*	*V_P/V_S*
1	1.2 (1.2)	2.25	1.88	1.89	1.3 (1.3)	2.46	2.06	1.73
2	1.1 (2.2)	3.12	3.13	1.76	0.7 (2.0)	3.03	2.90	1.81
3	3.7 (5.9)	3.44	3.36	1.81	2.1 (4.2)	3.34	3.44	1.77
4	4.1 (10.0)	3.60	3.56	1.73	13.6 (17.8)	3.60	3.58	1.81
5	14.2 (24.2)	3.59	3.70	1.80	9.3 (27.1)	3.51	3.64	1.73
6	12.5 (36.7)	3.91	4.19	1.72	9.6 (36.6)	3.91	4.10	1.67
7	12.7 (49.4)	4.46	4.45	1.70	8.2 (44.8)	4.46	4.51	1.74
	South-West RF Stack (SW)				**South East RF Stack (SE)**			
Layer	*Thickness (Depth) (km)*	*V_S top (km/s)*	*V_S base (km/s)*	*V_P/V_S*	*Thickness (Depth) (km)*	*V_S top (km/s)*	*V_S base (km/s)*	*V_P/V_S*
1	1.4 (1.4)	2.28	1.97	1.87	1.1 (1.1)	1.95	2.33	1.74
2	2.2 (3.7)	2.98	3.24	1.78	1.1 (2.2)	2.96	2.89	1.76
3	6.6 (10.3)	3.41	3.50	1.68	12.7 (15.0)	3.33	3.45	1.81
4	14.9 (25.2)	3.52	3.50	1.81	8.0 (23.0)	3.58	3.45	1.76
5	7.4 (32.6)	3.53	3.68	1.81	11.7 (34.7)	3.50	3.68	1.80
6	3.0 (35.6)	4.11	4.08	1.73	3.9 (38.6)	4.16	4.20	1.82
7	26.6 (62.2)	4.45	4.52	1.71	7.5 (46.2)	4.46	4.46	1.70

Table 2 – Best-fitting receiver function (RF) neighbourhood algorithm inversion results. Final velocity and thickness parameters are shown for each of the seven layers for each of the six regional RF stacks (V_P and V_S denote *P*- and *S*-wave velocity, respectively) (Figs. 2 and 3). Northwest and northeast stacks sample Istanbul-Zonguldak Zone (IZ) crust; central west and central east stacks sample Armutlu-Almacik (AA) block crust; south west and south east stacks sample Sakarya Zone (SZ) crust (Figs. 2 and 3).

692 **Figure Captions**

693

694 Figure 1 –Locations of seismometer stations for the DANA array (green triangles) and previous
695 seismic refraction experiments (as indicated in the legend), segments of the North Anatolian Fault
696 zone (red) and major tectonic terranes (IZ: Istanbul-Zonguldak zone; AA: Almatlu-Almacik zone;
697 and SZ: Sakarya zone). The inset map shows the regional tectonic setting.

698

699 Figure 2 – Earthquake locations and representative receiver function stacks. a) Earthquakes with
700 m_b>5.5, occurring during the deployment of the Dense Array for Northern Anatolia (DANA, yellow
701 circles) and since 2009 (permanent stations, orange circles) and within an epicentral distance
702 range of 30-90° (defined by red circles) were used for receiver function estimation. b) Selected
703 extended multi-taper receiver functions (MTRF) stacked by station for the DANA network (blank
704 regions show the 3 stations that did not contribute MTRFs). c) Regional MTRF stacks for the six
705 sub-regions identified in Figure 3.

706

707 Figure 3 – Topographical map of the study region with calculated piercing point locations of *P-S*
708 receiver function conversions at 35 km depth (using the IASP91 Earth velocity model of Kennett
709 and Engdahl (1991)) for selected source-receiver pairs (purple crosses). The major surface north
710 Anatolian fault (NAF) traces are marked in red with the Black Sea in the north and Sea of Marmara
711 to the west (shaded light blue). Labelled yellow rectangles denote the six sub-regions used to
712 construct receiver function stacks shown in Figure 2 and labelled thick black lines show the
713 locations of migrated receiver function profiles shown in Figure 6.

714

715 Figure 4 – Move-out corrected time domain receiver function stacks for the six sub-regions
716 indicated in Fig. 3). For each stack (a-f), semblance is plotted in *H* (crustal thickness) and *κ* (whole
717 crust V_P/V_S) space alongside raw receiver functions in sequence of increasing ray parameter.
718 Crustal thickness and V_P/V_S that produce maximum semblance of each stack and corresponding
719 receiver function phases (*Ps*, *PpPs* and *PpSs+PsPs*) are marked by a black star in *H-κ* space and
720 corresponding phases are plotted onto the receiver function sections. Secondary maxima are
721 shown with an open star.

722

723 Figure 5 – Neighbourhood algorithm (Sambridge, 1999) inversion results for the six regional
724 extended multi-taper receiver function (MTRF) stacks shown in Figure 3. The observed (black) and
725 synthetic (blue) receiver function waveforms for each stack are compared in the panels to the left
726 with chi-squared misfit values. Corresponding seven layer models are shown in the panels to the
727 right, with the best one thousand (yellow to green lines) models from 10001 iterations (grey lines).
728 The *S*-wave velocity and V_P/V_S values of the best overall model for each stack (red lines) are
729 displayed alongside a reference velocity model (blue lines) from a nearby seismic refraction
730 experiment (Bekler *et al.*, 2008). Horizontal black dashed lines denote the relevant H-*κ* stacking
731 depth result for each regional stack (Fig. 4). See text for inversion details.

732

733 Figure 6 – Representative south-north and west-east amplitude profiles (the locations of which are
734 shown in Figure 3) of 1.2 Hz time domain receiver functions (TDRF) migrated to 35 km (using the
735 inversion results in Figure 5). Superimposed are topography and seismicity within ~10 km of the
736 profile (black filled circles, Altuncu Poyraz *et al.*, 2015). Inverted green triangles denote stations

737 that contribute receiver functions to the migrated image and areas with less than 20 receiver
738 functions are shown in grey. The interpreted Moho (black dashed line), lower crustal positive *P-S*
739 conversion (red dotted line), near surface *P-S* conversion (white dotted line) and upper mantle
740 positive amplitudes (blue dash-dot line) are labelled, along with prominent regions of crustal (grey
741 dotted line) and upper mantle (orange dash-dot line) amplitudes. Major crustal terranes (SZ:
742 Sakarya Zone; AA: Armutlu-Almacik Zone; and IZ: Istanbul-Zonguldak Zone) and the locations of
743 the southern (SNAF) and northern (NNAF) branches of the north Anatolian fault are labelled. a)
744 western south-north profile; b) eastern south-north profile; c) southern west-east profile; d)
745 central west-east profile; and e) northern west-east profile.

746

747 Figure 7 – South-north schematic diagrams to illustrate the variations in crustal structure and
748 interpreted North Anatolian Fault zone structure in the eastern (a) and western (b) parts of the
749 study region. Sakarya Zone (SZ) crust displays two distinct structures (light and mid-grey) in the
750 western profile whilst its upper mantle (dark grey) is featureless and may also underlie the
751 Armutlu-Almacik (AA) crust (green). The Istanbul-Zonguldak Zone (IZ) crust (blue) and upper
752 mantle (purple) are separated by a weak Moho in the west and the locations of upper mantle
753 structures are highlighted (red hatching). The NNAF and SNAF (thick black dashed lines) are
754 interpreted to be sub-vertical on the western profile and to dip at ~65° to the north and south
755 respectively, on the eastern profile. Low velocity (LVZ) and high velocity (HVZ) zones are also
756 shown as candidate locations for decoupling within the crust, together with regions of notable
757 seismicity (Altuncu Poyraz *et al.*, 2015) (black hatching).

758

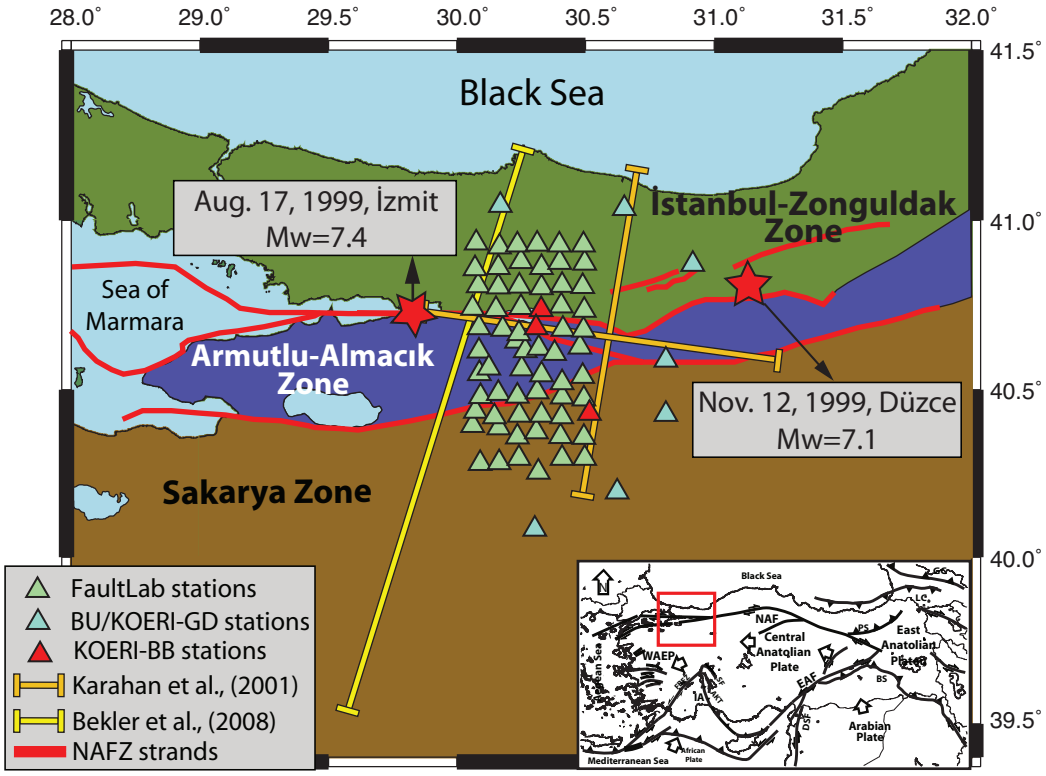
28.0°
29.0°
29.5°
30.0°
30.5°
31.0°
31.5°
32.0°
41.5°
41.0°
40.5°
40.0°
39.5°
Black Sea
Aug. 17, 1999, İzmit
Mw=7.4
İstanbul-Zonguldak
Zone
Sea of
Marmara
Armutlu-Almacık
Zone
Nov. 12, 1999, Düzce
Mw=7.1
Sakarya Zone
FaultLab stations
BU/KOERI-GD stations
KOERI-BB stations
Karahan et al., (2001)
Bekler et al., (2008)
NAFZ strands
Black Sea
NAF
Central
Anatolian
Plate
East
Anatolian
Plate
WAEP
EAF
DSF
Arabian
Plate
Mediterranean Sea

Figure 1

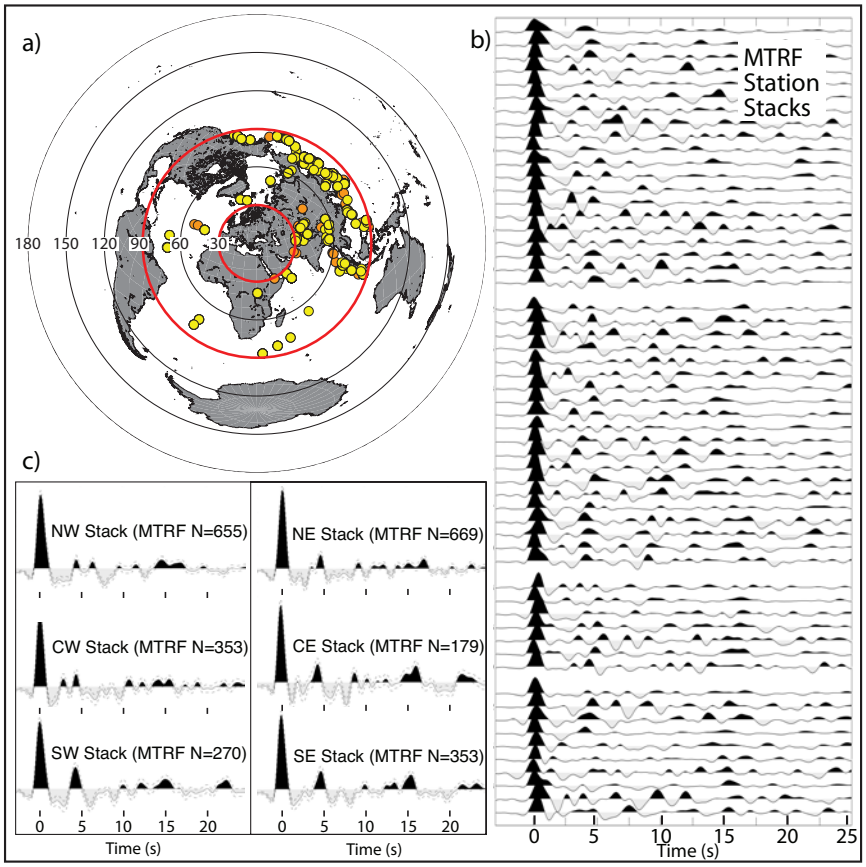
a)
180 150 120 90 60 30
b)
MTRF
Station
Stacks
0 5 10 15 20 25
Time (s)
c)
NW Stack (MTRF N=655)
CW Stack (MTRF N=353)
SW Stack (MTRF N=270)
NE Stack (MTRF N=669)
CE Stack (MTRF N=179)
SE Stack (MTRF N=353)
0 5 10 15 20
Time (s)
0 5 10 15 20
Time (s)

Figure 2

778

779

780

781

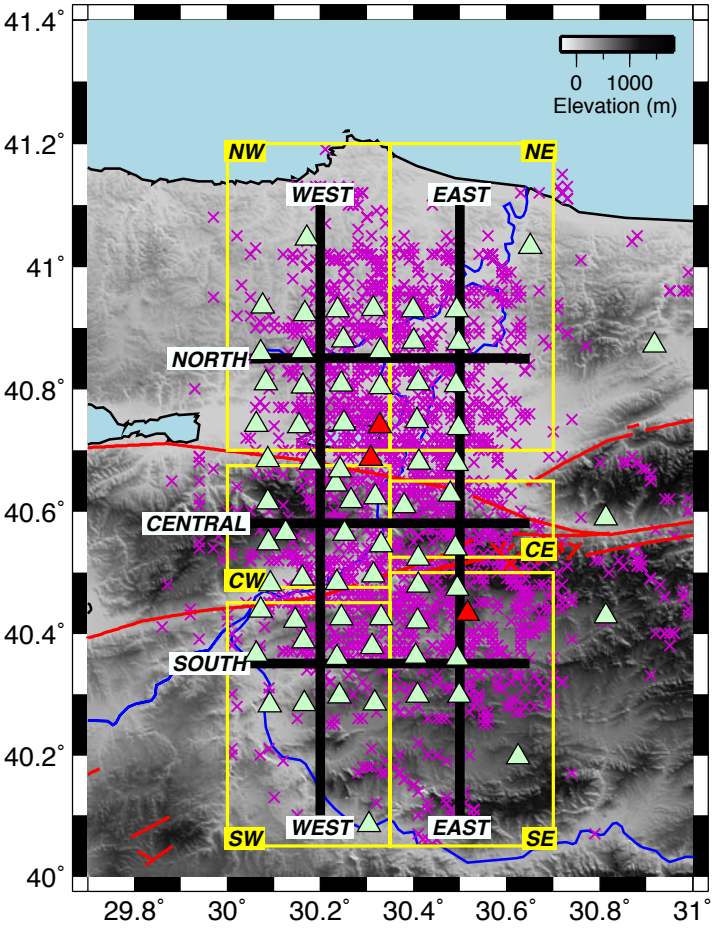

782

783

784 Figure 3

785

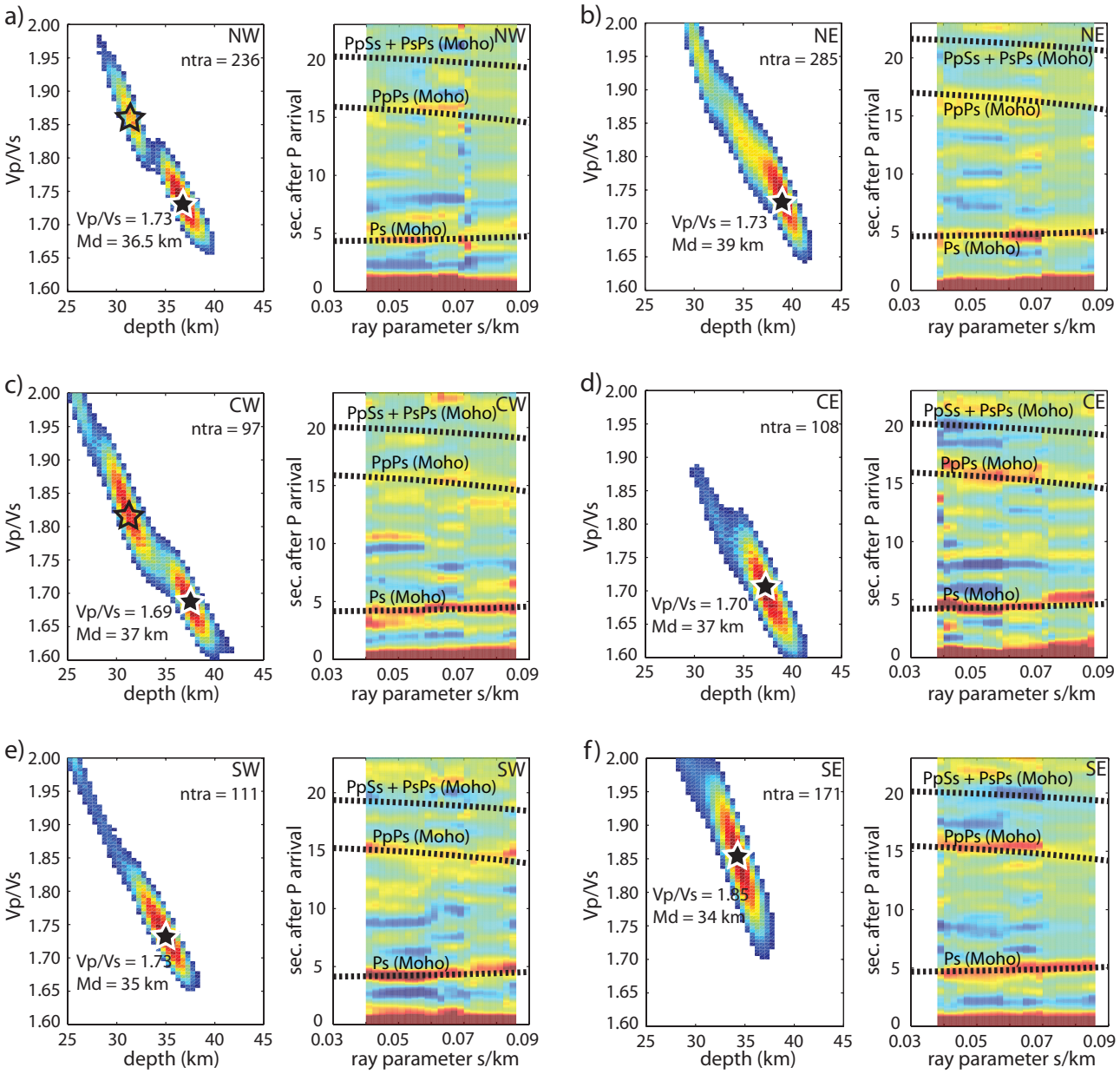
a)
NW
ntra = 236
Vp/Vs = 1.73
Md = 36.5 km
PpSs + PsPs (Moho)
PpPs (Moho)
Ps (Moho)
b)
NE
ntra = 285
Vp/Vs = 1.73
Md = 39 km
c)
CW
ntra = 97
Vp/Vs = 1.69
Md = 37 km
d)
CE
ntra = 108
Vp/Vs = 1.70
Md = 37 km
e)
SW
ntra = 111
Vp/Vs = 1.73
Md = 35 km
f)
SE
ntra = 171
Vp/Vs = 1.85
Md = 34 km
Vp/Vs
depth (km)
sec. after P arrival
ray parameter s/km

Figure 4

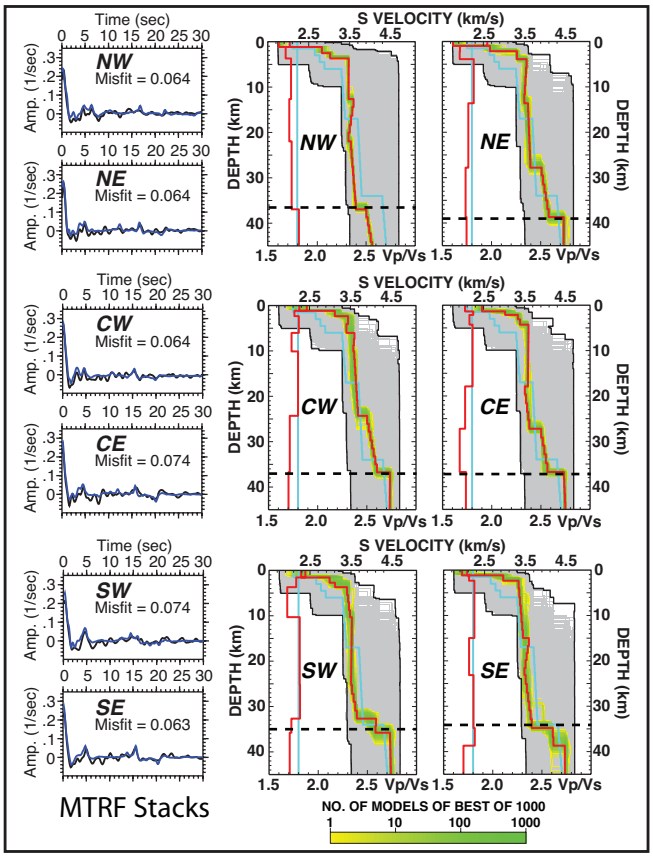
Time (sec)
S VELOCITY (km/s)
NW
Misfit = 0.064
NE
Misfit = 0.064
CW
Misfit = 0.064
CE
Misfit = 0.074
SW
Misfit = 0.074
SE
Misfit = 0.063
Amp. (1/sec)
DEPTH (km)
Vp/Vs
MTRF Stacks
NO. OF MODELS OF BEST OF 1000

Figure 5

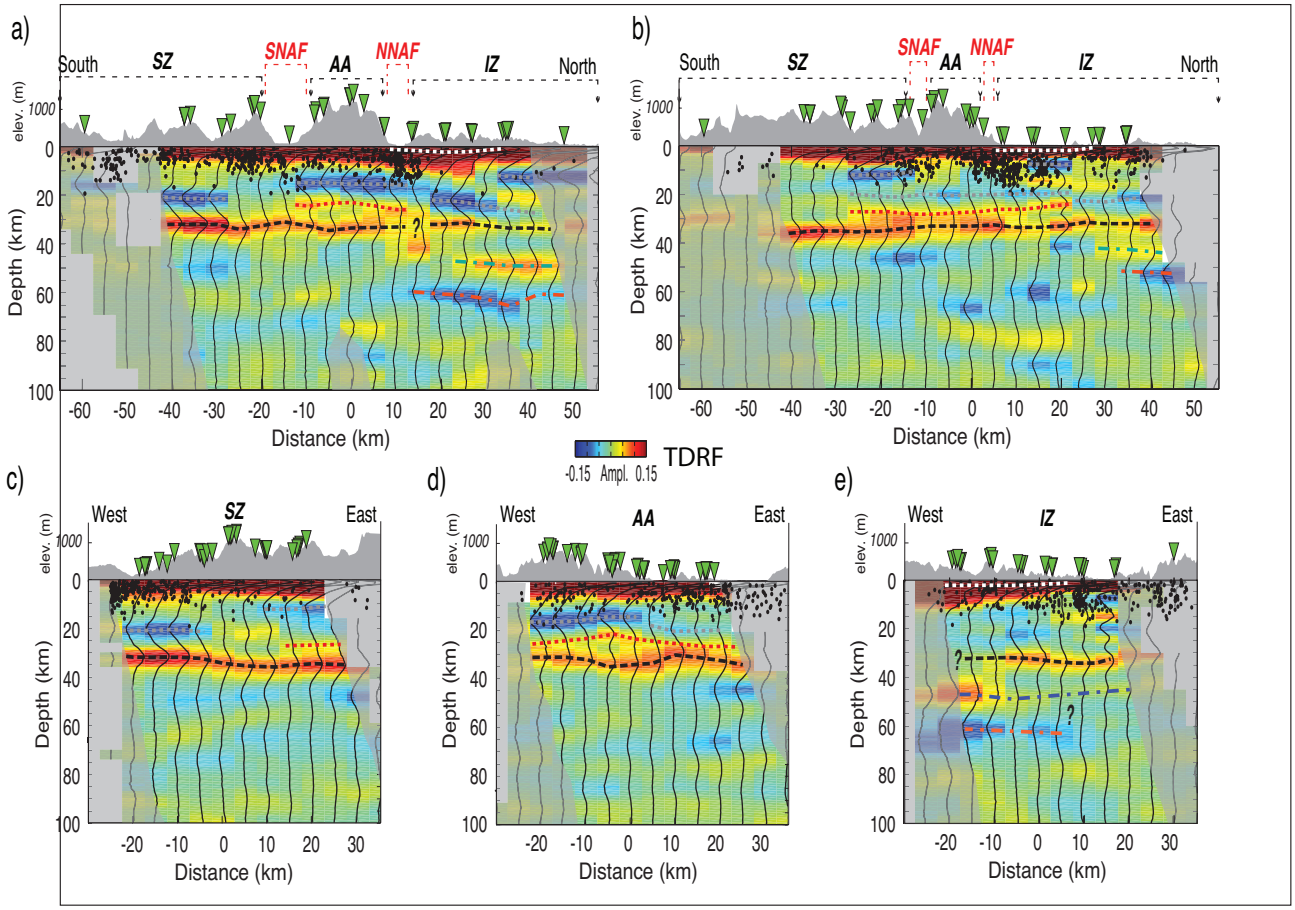
a)
South
SZ
SNAF
AA
NNAF
IZ
North
elev. (m)
1000
0
Depth (km)
20
40
60
80
100
-60 -50 -40 -30 -20 -10 0 10 20 30 40 50
Distance (km)
?
b)
South
SZ
SNAF
AA
NNAF
IZ
North
elev. (m)
1000
0
Depth (km)
20
40
60
80
100
-60 -50 -40 -30 -20 -10 0 10 20 30 40 50
Distance (km)
-0.15 Ampl. 0.15
TDRF
c)
West
SZ
East
elev. (m)
1000
0
Depth (km)
20
40
60
80
100
-20 -10 0 10 20 30
Distance (km)
d)
West
AA
East
elev. (m)
1000
0
Depth (km)
20
40
60
80
100
-20 -10 0 10 20 30
Distance (km)
e)
West
IZ
East
elev. (m)
1000
0
Depth (km)
20
40
60
80
100
-20 -10 0 10 20 30
Distance (km)
?
?

Figure 6

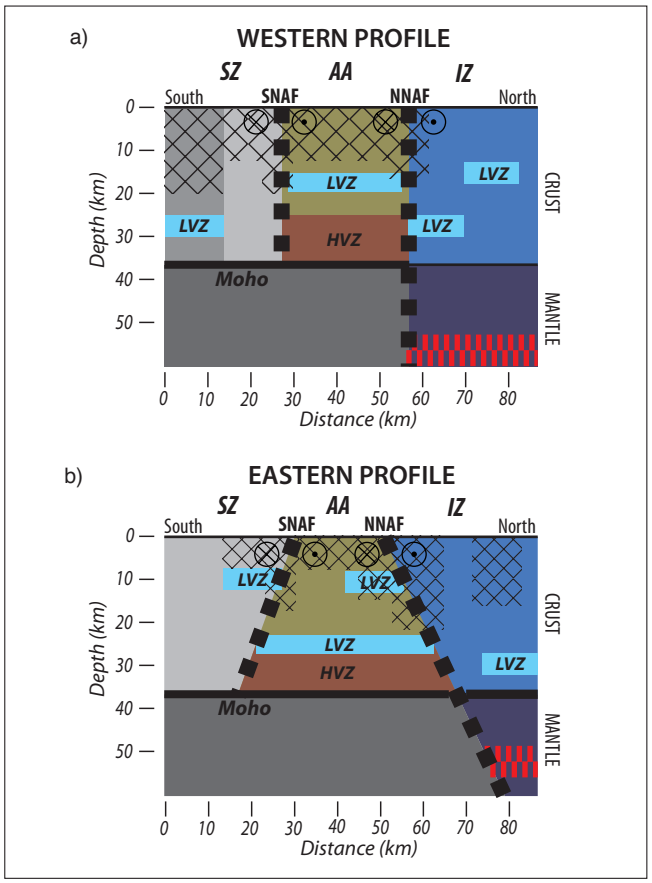
a)
WESTERN PROFILE
SZ
AA
IZ
South
SNAF
NNAF
North
LVZ
LVZ
LVZ
LVZ
HVZ
Moho
CRUST
MANTLE
Depth (km)
0
10
20
30
40
50
0
10
20
30
40
50
60
70
80
Distance (km)
b)
EASTERN PROFILE
SZ
AA
IZ
South
SNAF
NNAF
North
LVZ
LVZ
LVZ
LVZ
HVZ
Moho
CRUST
MANTLE
Depth (km)
0
10
20
30
40
50
0
10
20
30
40
50
60
70
80
Distance (km)

Figure 7

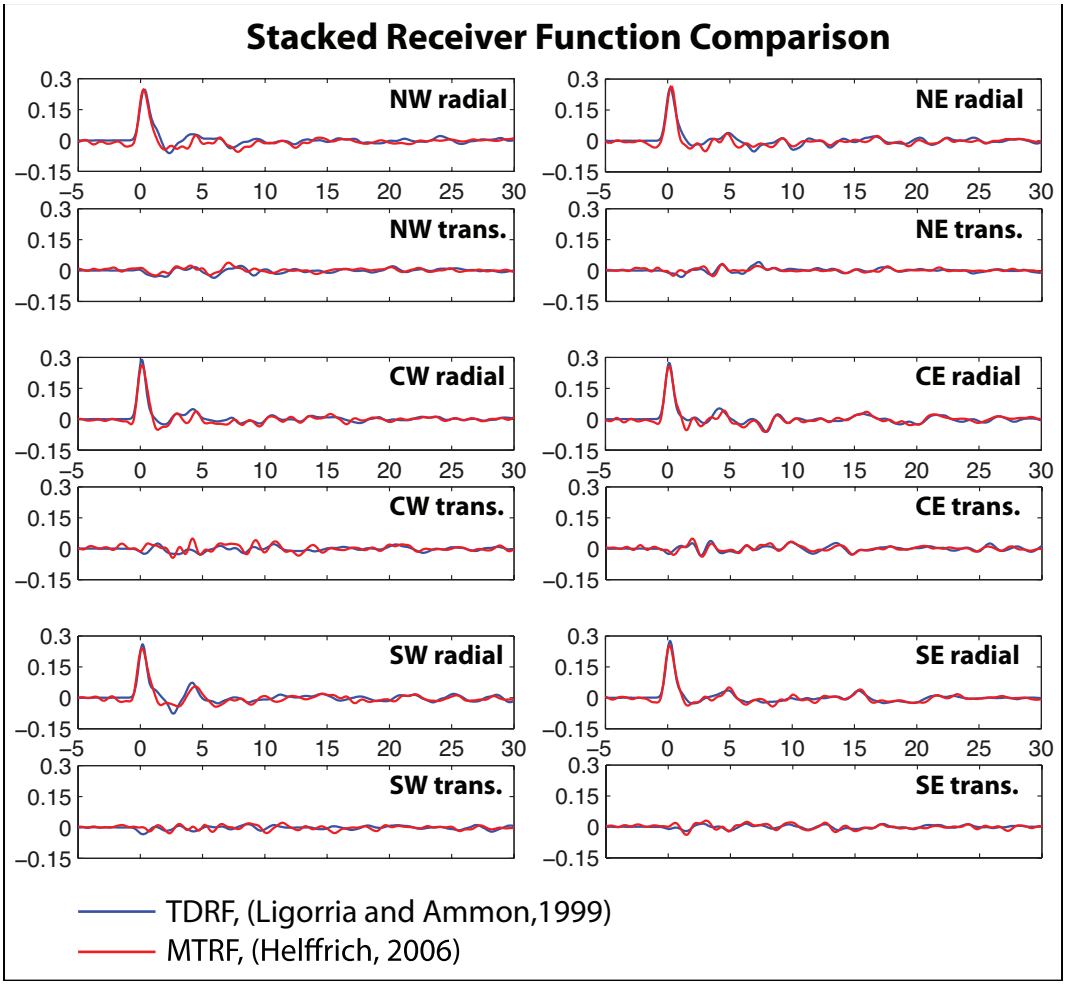

820

821

822 Supplementary Figure 1 – Comparison of the six regional stacks made using the time domain
823 (TDRF) (Ligorria and Ammon, 1999) and extended multi-taper (MTRF) (Helffrich, 2006) receiver
824 function calculation techniques. The main features are similar in each regional stack for both
825 calculation methods. Slight differences in both radial and transverse component receiver function
826 stacks are caused by: i) a different number of traces in each stack (TDRF=1363; MTRF=2479); ii)
827 variations in individual receiver function noise levels between calculation methods; and iii) an
828 observed marginal increase in frequency content in the MTRF dataset compared to the TDRF
829 dataset.

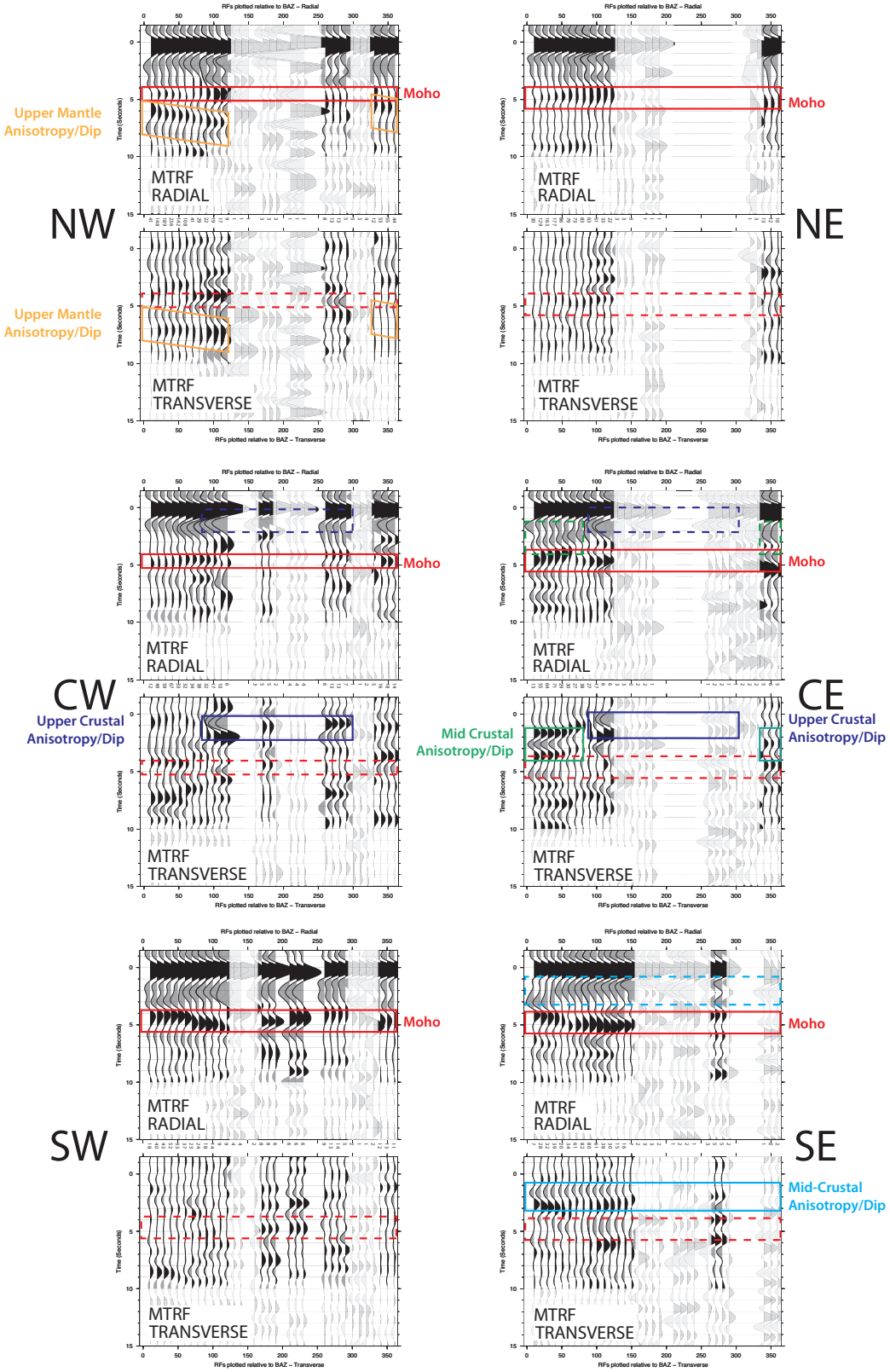

Supplementary Figure 2 – Extended multi-taper (MTRF) radial and transverse receiver functions, stacked in regional back-azimuthal bins of width 10°. Semi-opaque white areas show regions of poor back-azimuthal coverage (with less than 5 RFs in each azimuthal bin) and/or times where multiple energy may interfere with *P-S* converted energy.

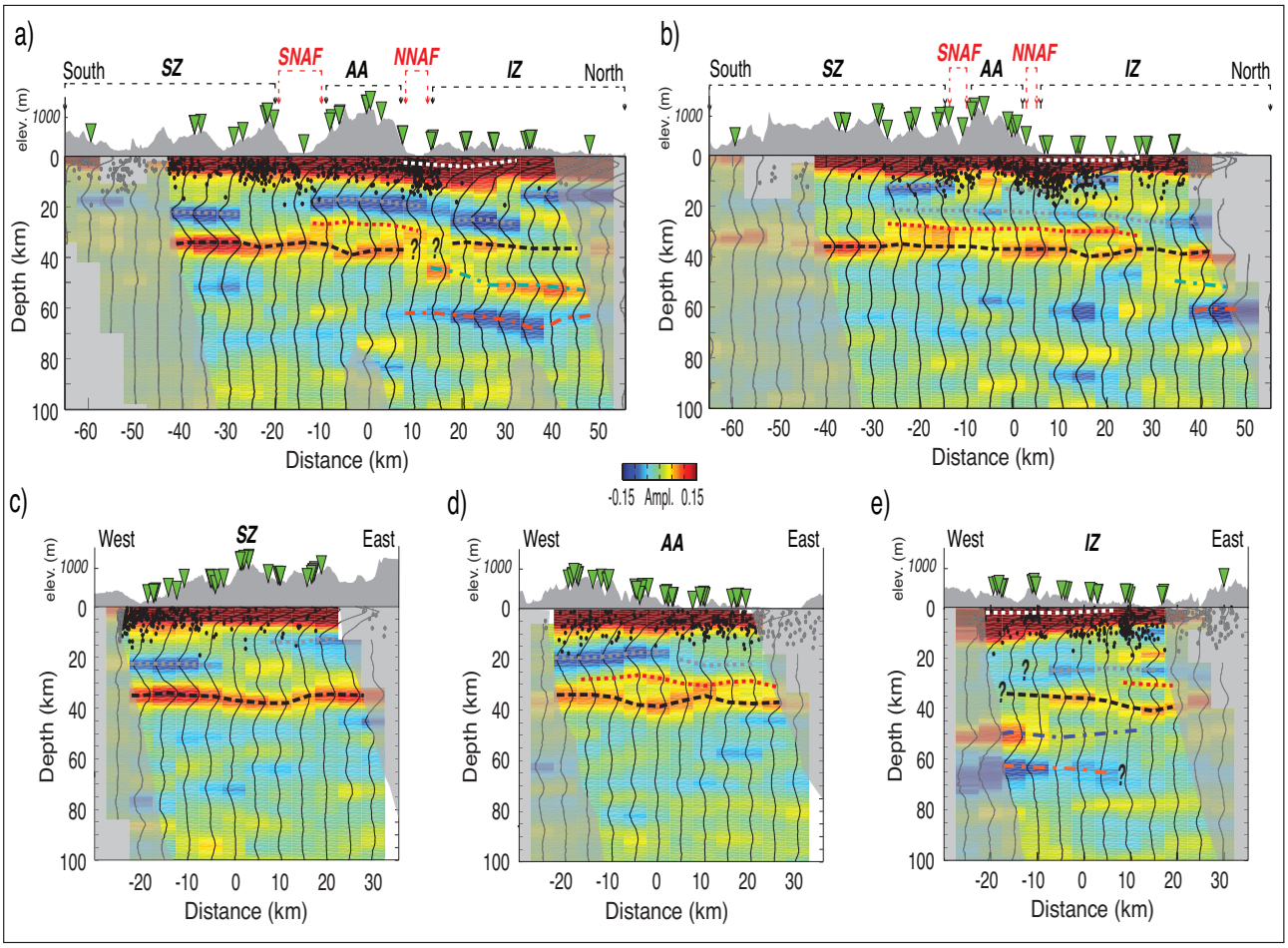

Supplementary Figure 3 – As Figure 6 in the manuscript but using a fixed velocity model of 6.2 km/s and a variable V_P/V_S, according to the regional H-κ stacking results.